Research Square

Preprints are preliminary reports that have not undergone peer review.
They should not be considered conclusive, used to inform clinical practice,
or referenced by the media as validated information.

Independent blazed diffraction in a polarization insensitive dual waveband metagrating

Ruoqian Gao

gaorq@sibet.ac.cn

Suzhou Institute of Biomedical Engineering and Technology of the Chinese Academy of Sciences
https://orcid.org/0009-0004-2191-9275

Xinran Su

Suzhou Institute of Biomedical Engineering and Technology of the Chinese Academy of Sciences

Pengtao Hu

Suzhou Institute of Biomedical Engineering and Technology of the Chinese Academy of Sciences

Kai Wu

Soochow University

Yingge Cong

Suzhou Institute of Biomedical Engineering and Technology of the Chinese Academy of Sciences

Junlin Li

Suzhou Institute of Biomedical Engineering and Technology of the Chinese Academy of Sciences

Mingfeng Ge

Suzhou Institute of Biomedical Engineering and Technology of the Chinese Academy of Sciences

Xiaoyi Liu

Soochow University

Wenfei Dong

Suzhou Institute of Biomedical Engineering and Technology of the Chinese Academy of Sciences

Article

Keywords:

Posted Date: March 4th, 2026

DOI: https://doi.org/10.21203/rs.3.rs-8988307/v1

License: This work is licensed under a Creative Commons Attribution 4.0 International License.
Read Full License

Additional Declarations: There is no conflict of interest

Title page

Independent blazed diffraction in a polarization insensitive dual waveband metagrating

Xinran Su[1], Pengtao Hu[1], Kai Wu[3,4],Yingge Cong[1] ,Junlin Li[1], Mingfeng Ge[1,*], Xiaoyi Liu[3,4,*], Ruoqian Gao[1,2,*], Wenfei Dong[1]

[1]Department of Biomaterials and Stem Cells,Suzhou Institute of Biomedical Engineering and Technology, Chinese Academy of Science, Suzhou 215163, China

[2]CAS Key Lab of Bio-Medical Diagnostics, Suzhou Institute of Biomedical Engineering and Technology, Chinese Academy of Sciences, Suzhou, Jiangsu 215163, China

[3]School of Optoelectronic Science and Engineering & Collaborative Innovation Center of Suzhou Nano Science and Technology, Soochow University, Suzhou 215006, China;

[4]Key Lab of Advanced Optical Manufacturing Technologies of Jiangsu Province & Key Lab of Modern Optical Technologies of Education Ministry of China, Soochow University, Suzhou 215006, China;

[*]Corresponding email: gemf@sibet.ac.cn;xyliu@suda.edu.cn; gaorq@sibet.ac.cn;

Abstract

Blazed gratings play a vital role in wavelength dispersion and directional beam steering, and the emergence of metasurfaces has opened new opportunities for compact and flexible blazed diffraction devices.However, whether in conventional or metasurface-based implementations, achieving stable and mutually independent wavefront responses under multi-wavelength operation remains a significant challenge.This work presents a metagrating design strategy that enables independent control of blazed diffraction across multiple wavelength bands, providing broadband wavefront manipulation within a single device. By arranging different circularly symmetric nanopillar units in an interleaved manner within a single planar layer and tuning the phase coverage for each wavelength band, multiple blazed diffraction modes can be achieved within a single device, with phase responses remaining independent across different bands. Such all-dielectric metagratings exhibit blazed diffraction behavior consistent with the design across both the visible and near-infrared bands, such all-dielectric metagratings exhibit blazed diffraction behavior consistent with the design across both the visible and near-infrared bands, with more than 90% of the transmitted energy concentrated in the designed diffraction orders. This work provides a compact and scalable design framework for multi-wavelength diffractive optical devices, with potential applications in planar optical systems.

Introduction

Blazed gratings are fundamental optical components for wavelength dispersion and beam steering, and they play an important role in spectral analysis, hyperspectral imaging, and optical communications[1-5]. However, the performance of conventional blazed gratings is fundamentally limited by their geometric configuration and material dispersion. Concretely,a blaze angle optimized for a specific central wavelength usually fails to maintain high diffraction efficiency at other wavelengths[6], while, the asymmetric groove

structures also have high requirements for fabrication accuracy[7-10]. These factors inevitably result in restrictions of conventional blazed gratings in terms of wideband adaptability and developing cost control[11].

In recent years, metasurfaces-based on two-dimensional subwavelength artificial structures have enabled flexible control of the optical phase[12-14], amplitude[15,16], and polarization[17-19] using on ultrathin platforms[20-22], providing a new design paradigm for miniaturized and functionally integrated optical devices[23-28]. With the continuous development of metasurface technology, the concept of metagratings occurs[29-34], which enhances selected diffraction orders by tailoring discrete diffraction channels within an extended supercell rather than reconstructing a continuous phase profile at an interface[35-38]. Consequently, the design paradigm of planar diffractive devices has shifted from continuous wavefront shaping to explicit diffraction-order energy allocation. This provides a more suitable theoretical basis for realizing high-efficiency blazed diffraction on ultrathin platforms[39,40].

Over the past years, extensive efforts have been devoted to improving the diffraction efficiency and diffraction-order controllability of planar blazed metasurfaces based on metagrating concepts and dispersion engineering. [41,42]. Nevertheless, most existing approaches are mainly restricted to globally wavelength-evolving diffraction-order distributions or designs optimized for a single spectral region. The former makes it difficult to independently prescribe diffraction orders across separated spectral bands, whereas the latter limits multi-band functionality and spectral scalability. In addition, multilayer architectures separate phase and amplitude modulation into different layers. This usually increases fabrication complexity and makes layer-to-layer alignment more demanding[43-46]. Therefore, it is still highly desirable to develop compact single-layer planar metasurfaces that can simultaneously achieve polarization-insensitive operation and independently tailored diffraction-order control across distinct spectral bands[47,48].

Here we propose a blazed metagrating design strategy for broadband, polarization-insensitive wavefront control. We propose a single-layer, all-dielectric metagrating strategy that enables independent blazed diffraction control across different spectral bands.By exploiting the intrinsic dispersion of circularly symmetric silicon nanopillars and independently engineering the phase coverage in each band through an interleaved layout, polarization-insensitive and cross-band diffraction-order decoupling is achieved within a single planar structure.Both simulations and experiments demonstrate distinctly different blazed diffraction behaviors in the visible and near-infrared bands, with more than 90% of the transmitted energy concentrated in the designed diffraction orders

(0th and −1st orders in the visible band and the +1st order in the near-infrared band).This compact and scalable design provides a practical route for multi-channel beam steering and wavefront manipulation in integrated and multi-spectral optical systems.. It provides a feasible route toward integrated multifunctional planar diffractive devices.

Results

Theory and principle

To achieve controlled beam deflection on the transmission side, this work designs a single-layer all-dielectric metagrating composed of subwavelength silicon nanopillars. By spatially tailoring the geometric parameters of the nanopillar units, the metagrating introduces a designed local phase response. This forms an effective phase-gradient distribution, which redirects the transmitted light into the desired diffraction channels. The basic operating principle is illustrated in Fig. 1a. At two representative wavelengths (λ_1 and λ_2), the structure produces anomalous deflection toward different diffraction orders. The corresponding far-field diffraction patterns are shown in the inset.From a far-field perspective, the diffraction behavior of the structure can be equivalently described as that of a blazed grating with an effective period d. The m-th transmitted diffraction order satisfies the general grating equation:

$$n_t \sin\theta_m - n_i \sin\theta_i = m\frac{\lambda_0}{d} \quad (1)$$

Here, n_i and n_t denote the refractive indices of the incident and transmission media, respectively. θ_i is the incidence angle, and θ_m is the exit angle of the m-th diffraction order measured with respect to the surface normal. λ_0 denotes the vacuum wavelength. This relation indicates that, under fixed incidence conditions, the effective period d determines the discrete diffraction channels that can be excited and their angular positions. The core of the device design is to further control the energy distribution among these channels, thereby enhancing the desired diffraction orders.From a phase-engineering perspective, blazed control of a target diffraction order m requires constructing an approximately linear phase ramp within one effective period. This ensures coherent addition of that order in the far field. The corresponding target phase profile can be expressed as:

$$\phi(x) = \frac{2\pi m}{d}x + \phi_0 \quad (2)$$

Here, ϕ_0 denotes the initial phase. The resulting phase gradient is given by

$$\frac{d\Phi}{dx} = \frac{2\pi m}{d} \quad (3)$$

By substituting this phase gradient into the generalized Snell's law[49]:

$$n_t \sin\theta_m - n_i \sin\theta_i = \frac{\lambda_0}{2\pi}\frac{d\Phi}{dx} \quad (4)$$

It can be seen that this expression is mathematically equivalent to the grating equation. The phase ramp provides an exact transverse momentum compensation for the transmitted wave, thereby coupling energy into the discrete m-th diffraction order. The difference lies in emphasis. The grating equation describes the discrete selection of diffraction orders, whereas phase engineering is used to direct energy concentration among these channels, giving rise to the blazed effect.

In practical metasurface implementations, a continuous phase ramp is usually approximated by a finite number of discrete elements. If an effective supercell contains Nnanopillar units, the phase step between adjacent units is given by:

$$\Delta\phi = \frac{2\pi m}{N} \quad (5)$$

When N is sufficiently large and the transmission amplitude remains smooth, discretization errors are effectively suppressed. Under these conditions, coherent addition in the target diffraction order approaches the ideal blazed regime, leading to a significant enhancement in diffraction efficiency. Therefore, achieving near-complete $0–2\pi$ phase coverage within one supercell is a necessary condition for high-efficiency blazed diffraction.

To systematically evaluate the phase modulation capability and transmission characteristics of the meta-units, a parametric sweep was performed for silicon nanopillars with diameters ranging from 50 to 150 nm. Pillar heights of 770 nm, 780 nm, 790 nm, and 800 nm were selected as representative cases for comparison. Simulation results show that, within both target operating bands, the meta-units exhibit clear and continuous propagation-phase responses. The overall phase coverage approaches a complete $0–2\pi$, providing a structural basis for subsequent blazed order engineering.As shown in Fig. 1b, phase-gradient units designed for different operating bands are not arranged using conventional spatial partitioning. Instead, they are interleaved and embedded within the same structure along the phase-gradient direction. With this alternating arrangement, adjacent silicon nanopillars differ significantly in both geometry and phase response. As a result, the two sets of functional units are spatially interleaved. Building on this arrangement, a lateral displacement on the order of half a period is further introduced. This

shift breaks the strict alignment of different functional units along the phase-gradient direction, resulting in a staggered interleaved layout.

The key role of this arrangement is to enable band-selective phase modulation. As shown in Fig. 1c, in the 970–1010 nm band, nanopillar units optimized for this band exhibit pronounced phase dispersion. Their transmission phase varies monotonically along the unit sequence, forming an approximately linear phase gradient. In contrast, units originally designed for the 620–660 nm band show only weak phase variation in this wavelength range and can be regarded as a nearly flat-phase group. These units mainly provide spatial filling and amplitude smoothing. Consequently, the phase variation of the background group is much smaller than the phase gradient introduced by the modulation group and does not alter the selection or energy concentration of the dominant diffraction order. In this case, the overall effective phase distribution is dominated by the phase-modulation group. Near-complete 2π phase coverage is achieved within the extended effective grating period, resulting in unidirectional blazed diffraction.When the operating band switches to 620–660 nm, the functional roles of the two unit groups are exchanged due to their structural dispersion characteristics. Units that previously served as the phase-background group exhibit strong phase modulation in this band and form a new phase gradient in the opposite direction. In contrast, units originally designed for the near-infrared band reduce to an approximately flat-phase group. Because opposite phase-gradient directions are assigned to the two unit groups, the main diffraction directions at different bands are effectively separated in space.

This staggered interleaved structure does not simply superimpose two phase profiles. Instead, it exploits band-selective responses induced by structural dispersion, allowing different functional units to dominate in different operating bands. At a given spectral band, only one unit group provides a significant spatial phase variation, while the other acts as an approximately uniform phase background with a minimal impact on the overall phase gradient. Meanwhile, the staggered arrangement increases the spatial spacing between the units that actively contribute to phase modulation, thereby introducing a longer modulation scale. This arrangement suppresses energy leakage into non-target diffraction orders and concentrates the transmitted energy more efficiently into the desired order. Unlike conventional metasurfaces that rely on gradual changes between adjacent units, the diffraction behavior in this structure is governed by spatially separated functional units. As a result, the diffraction angles and energy distribution are mainly determined by the overall repetition period formed by these spaced units and are insensitive to the local arrangement between adjacent elements.Accordingly, the staggered interleaved structure can be regarded as a nested blazed metagrating selectively activated

by structural dispersion. By enabling alternating activation of phase-modulation channels at different spectral bands within a single planar layer, this design provides an efficient and scalable route for coordinated dual-band blazed diffraction control.

Wavelength-dependent blazing behavior and diffraction order engineering

While keeping the phase-gradient construction and the staggered interleaved layout unchanged, the phase coverage in different operating bands can be continuously tuned by adjusting the geometric parameter combinations of the silicon nanopillars. This effectively modifies the distribution of transmitted energy among diffraction channels in the far field. Figures 2a, c, and e show the relative transmission phase distributions of three representative designs in the visible band (620–660 nm) and the near-infrared band (970–1010 nm). In different blazed operating modes, each functional unit group exhibits an approximately flat phase response in its non-design band and acts as a phase background (see Supporting Information Section Fig.S1-S3). The corresponding far-field angular distributions are presented in Figs. 2b, d, and f. Here, λ=640 nm and λ=990 nm are selected as representative wavelengths for the two operating bands, respectively, far-field angular distributions at other wavelengths are provided in the Supporting Information Figs. S4–S6.

When near-complete 0–2π phase coverage is achieved in both operating bands (Figs. 2a, b), the transmitted energy is mainly concentrated in the −1st diffraction order at $\lambda = 640$ nm. In contrast, at $\lambda = 990$nm, the transmitted energy is predominantly directed into the +1st order. In this case, both bands exhibit typical single-blaze behavior, corresponding to a dual-band single-blaze operating state. Moreover, the blazing order in each band can be independently prescribed; a design exhibiting −1st order blazing in both bands is further provided in the Supporting Information (Fig. S7).By contrast, upon reducing the phase coverage in the visible band while preserving a nearly ideal linear phase gradient in the near-infrared band (Figs. 2c, d), the transmitted energy at $\lambda = 640$ nm is distributed between the 0th and −1st diffraction orders. This produces a stable dual-lobe far-field pattern, corresponding to a partial-blaze behavior. Meanwhile, at $\lambda = 990$ nm, a single-blaze response into the +1st order is maintained. This case represents a hybrid blazed operating mode.With further adjustment of the unit parameters, the phase coverage in both operating bands becomes insufficient to support single-channel blazing (Figs. 2e, f). Under these conditions, at $\lambda = 640$ nm and $\lambda = 990$ nm, the transmitted energy is redistributed between the 0th order and the corresponding anomalous diffraction orders. As a result, both bands exhibit stable partial-blaze behavior, corresponding to a dual-band partial-blaze operating state.

Taken together, these results demonstrate that the interleaved–staggered composite phase-gradient metagrating preserves a fixed anomalous deflection direction while enabling a continuous transition from single-blaze to partial-blaze behavior through phase-coverage tuning. Different blazed operating states can be flexibly combined across the two spectral bands. The partial-blaze state originates from deliberate control of the phase coverage in different operating bands. It reflects a controlled redistribution of transmitted energy among multiple diffraction channels, rather than a failure of the phase gradient or random scattering effects. This characteristic demonstrates that the proposed metagrating structure enables flexible and programmable dual-band energy control.Based on these considerations, the hybrid blazed operating mode is selected for experimental validation in this work. In this mode, a single anomalous deflection channel is stably maintained in one operating band, while dual-channel energy distribution appears in the other band. This allows a single device to simultaneously demonstrate band-selective blazed behavior and far-field energy control, offering high experimental observability and validation value.

Fabrication and Characterization

To verify the feasibility of the proposed design, the metagrating samples were fabricated on a silicon-on-sapphire (SOS) substrate. The overall fabrication process is illustrated in Fig. 3a and consists of five main steps: spin coating of an electron-beam resist, pattern definition by electron-beam lithography (EBL), chromium (Cr) hard-mask deposition, inductively coupled plasma (ICP) etching, and subsequent resist removal. Specifically, an electron-beam resist was first spin-coated onto the SOS substrate and patterned by EBL exposure and development to define the designed silicon nanopillar array. A thin chromium layer was then deposited as a hard mask, and the pattern was transferred into the silicon layer by ICP etching with high anisotropy. Finally, the chromium mask and residual resist were removed, yielding a periodic silicon nanopillar metagrating on the sapphire substrate. A macroscopic photograph of the fabricated metagrating sample is provided in the Supporting Information Fig. S8.

The fabricated samples were structurally characterized using scanning electron microscopy (SEM). As shown in Fig. 3b, the metagrating exhibits good periodic uniformity and structural integrity over a large area. The enlarged top-view SEM image in Fig. 3c further confirms that the silicon nanopillars are well defined, with pillar diameters and array spacing consistent with the design parameters. The tilted-view SEM image in Fig. 3d shows that the nanopillars have nearly vertical sidewalls and smooth surfaces, with no obvious collapse or lateral etching observed. This confirms the high precision and fidelity of the fabrication process.These results confirm that the proposed dual-band

metagrating structure is readily realizable using practical fabrication processes and is highly compatible with standard nanofabrication techniques. This provides a reliable experimental basis for further applications in integrated photonics and planar optical systems.

Experimental Demonstration

To characterize the diffraction response of the interleaved–staggered metagrating over a broad spectral range, an optical measurement setup was constructed, as shown in Fig. 4(a). In the experiment, monochromatic light from a tunable source was collimated and then directed to normally illuminate the metagrating sample through an aperture and a microscope objective. The transmitted diffraction spots were collected by an imaging system and recorded using a CCD camera, enabling systematic characterization of the diffraction behavior at different wavelengths.Figure 4b shows representative transmitted diffraction patterns measured in the visible and near-infrared ranges, corresponding to the 620–660 nm and 960–1010 nm bands, respectively. In the visible band (620–660 nm), the transmitted energy is mainly distributed between the −1st and 0th diffraction orders, forming two dominant spots with comparable intensity and corresponding to a partial-blaze mode. In contrast, in the near-infrared band (960–1010 nm), the transmitted energy is strongly concentrated in the +1st order, exhibiting a clear single-blaze behavior. These experimental observations are consistent with the numerical simulation results, indicating that the designed interleaved–staggered metagrating enables band-dependent diffraction-order selection and energy control. All measured two-dimensional diffraction patterns over the 570–1050 nm wavelength range are provided in the Supporting Information Fig. S9.

To further quantify the distribution of transmitted energy among different diffraction orders, Fig. 4c presents the experimentally measured diffraction efficiencies of the −1st, 0th, and +1st orders as functions of wavelength. For comparison with the design targets, the primary operating wavelength ranges selected during the design stage are highlighted in Fig. 4c using shaded regions of different colors. It can be seen that in the visible band (620–660 nm, indicated by the red shaded region), the diffraction efficiencies of the −1st and 0th orders remain consistently high, while the +1st-order efficiency is relatively low. This indicates that the transmitted energy is mainly distributed between the −1st and 0th channels, corresponding to a hybrid blazed operating state. As the wavelength gradually deviates from the designed band, the energy distribution among the diffraction orders changes, reflecting the influence of dispersion in the unit phase response on the diffraction efficiency.In contrast, in the near-infrared band (960–1010 nm, indicated by the blue shaded region), the +1st-order diffraction efficiency is significantly enhanced and becomes

dominant, while the −1st and 0th orders are strongly suppressed. This indicates a stable single-channel blazed deflection behavior in this band. These experimental results are in good agreement with the phase-gradient design and far-field simulation predictions, validating the effectiveness of the dual-band opposite-order control strategy from an energy-distribution perspective.

Figure 4d provides a quantitative analysis of the wavelength-dependent spatial displacement of the −1st and +1st diffraction spots relative to the 0th-order spot. The left axis shows the experimentally extracted relative displacement of the diffraction spots in pixels, while the right axis corresponds to the theoretically calculated values of $\tan\theta_m$, which quantify the expected displacement of the diffraction spots. The detailed calculation procedure for $\tan\theta_m$ is provided in the Supporting Information, as given in Equation (S1).It can be observed that the measured wavelength-dependent displacements of the −1st and +1st diffraction spots relative to the 0th order are in good agreement with the theoretical calculations. This indicates that the dispersive deflection behavior of the device is mainly determined by the effective grating period introduced by the staggered layout. This result further confirms that the interleaved–staggered structure can be equivalently described as a blazed metagrating in the far field, whose diffraction behavior follows the grating momentum relation.

Discussion

In summary, we propose and experimentally demonstrate a dual-band blazed metagrating design based on phase-coverage control. On a single-layer, all-dielectric, and polarization-insensitive platform, this approach employs an interleaved–staggered arrangement of phase-gradient units to independently control the phase coverage in different operating bands. As a result, multiple diffraction states—including single-blaze, partial-blaze, and hybrid-blaze behaviors—can be realized within a single device.Within this design framework, when near-complete 0–2π phase coverage is achieved in a given operating band, the transmitted energy is primarily concentrated into a single target diffraction order, resulting in single-order blazing. When the phase coverage is reduced, the transmitted energy is redistributed in an ordered manner between the 0th order and anomalous diffraction orders, giving rise to stable partial-blaze or multi-channel blazed behavior. Numerical simulations systematically verify the feasibility of these different blazed states under dual-band operation. Considering experimental observability and measurement stability, the hybrid blazed operating state was selected for experimental validation. The experimental results are in good agreement with the simulation predictions.Both experiments and simulations confirm that this approach enables independent cross-band diffraction-order control on a compact single-layer dielectric

platform, without multilayer stacking. The interleaved–staggered arrangement also suppresses undesired diffraction components and improves the stability of multiband operation at the effective supercell scale.The proposed design methodology is general and can be extended to dual-band beam splitting, wavelength-selective beam deflection, and related planar optical devices, providing a feasible design route for multiband integrated photonic systems.

Materials and methods

Numerical simulations

Numerical simulations of the metagrating were performed using the commercial software Lumerical FDTD Solutions (2023 R2). The simulation model was constructed based on a three-dimensional unit-cell structure. Periodic boundary conditions were applied along the $x$and $y$directions to represent the two-dimensional in-plane periodicity of the metasurface. Perfectly matched layers (PMLs) were employed above and below the structure along the propagation (z) direction to absorb outgoing electromagnetic waves and eliminate boundary reflections.For material parameters, the refractive index of the silicon nanopillars was taken from experimentally measured dispersion data, while the refractive index of the sapphire substrate was adopted from a widely used optical constants model reported in the literature. All simulations employed frequency-domain monitors to extract the transmission phase and far-field distributions, which were used to analyze the diffraction-order distribution and blazed behavior at different wavelengths.

Superficial manufacturing

A $\approx$220 nm thick layer of polymethyl methacrylate (PMMA) electron-beam resist was spin-coated at 4000 rpm for 60 s onto a crystalline silicon-on-sapphire (SOS) substrate (800 nm c-Si/475 μm sapphire). The metagrating pattern was exposed via electron-beam lithography (EBL) at 220 μC cm^{-2}, 20 kV, and 76 pA. Development was carried out in a methyl isobutyl ketone and isopropanol (MIBK:IPA 1:3) solution for 60 s. Subsequently, a 40 nm thick chromium (Cr) hard mask was deposited by electron-beam evaporation (AdNaNo, EBS-150), and the mask pattern was defined via lift-off. The Si nanopillars were then etched using inductively coupled plasma (ICP) with C_4F_8 (80 sccm), SF_6 (60 sccm), and O_2 (5 sccm) at 800 W ICP power and 35 W RF power for 80 s. Finally, the Cr mask was removed with a chromium etchant to obtain the final Si metagrating.

Optical measurements with a microscopy system

The experimental setup included broadband diffraction measurements performed using a 320 mm imaging-corrected spectrometer (Omni-3007i) coupled with a tunable monochromatic light source (TLS3-T250A-GJS) covering 350–2400 nm. Collimated light was normally incident on the metagrating, and the transmitted diffraction patterns were recorded by a CCD, providing a spectral resolution of 0.12 nm.

Acknowledgements

We acknowledge support from the National Key R&D Program of China (Grant No. 2024YFF0618201), the Youth Innovation Promotion Association of CAS(Grant No. 2023338).

Author details

1Department of Biomaterials and Stem Cells,Suzhou Institute of Biomedical Engineering and Technology, Chinese Academy of Science, Suzhou, China.2School of Optoelectronic Science and Engineering, Soochow University, Suzhou, China.

Author Contributions

R.G. conceived the idea. X.S. developed the metagrating simulation and sample fabrication, set up the experiment, and authored the manuscript.Y.C., P.H. and J.L. carried out the measurements. X.L. and K.W. fabricated the sample, W.D., X.L.,M.G. and R.G. improved the idea, R.G. and X.S. supervised the overall project. All of the authors analyzed the data and discussed the results.

Data availability

The data that support the findings of this study are available from the corresponding authors upon reasonable request.

Conflict of interest

The authors declare no competing interests.

References

1. Luan, M. et al. Elliptical vibration ruling of orientation-tuneable blazed gratings for high-flexibility fabrication of structural colours. J. Mater. Process. Technol. 337, 118729 (2025).

2. Zhang, Z. et al. Improving the optical subdivision ability of a grating interferometer via double-row reverse blazed gratings. Opt. Lasers Eng. 168, 107676 (2023).

3. Zhang, Z. et al. Achieving high-fold optical subdivision of a blazed grating interferometer through near-Littrow incidence. IEEE Trans. Instrum. Meas. (2025).

4. Wang, J., Wang, Y., Zhang, J., Schulze, V. & Guo, P. Blazed grating enables highly decoupled optically variable devices fabricated by vibration-assisted diamond texturing. Opt. Express 30, 8829-8846 (2022).

5. Mattelin, M.-A., Radosavljevic, A., Missinne, J., Cuypers, D. & Van Steenberge, G. Design and fabrication of blazed gratings for a waveguide-type head mounted display. Opt. Express 28, 11175-11190 (2020).

6. Baldry, I. K., Bland-Hawthorn, J. & Robertson, J. Volume phase holographic gratings: polarization properties and diffraction efficiency. Publ. Astron. Soc. Pac. 116, 403 (2004).

7. Chen, Z. et al. High-precision and high-efficiency fabrication of blazed grating by ultrasonic-assisted ultraprecision planing. J. Mater. Process. Technol. 311, 117802 (2023).

8. Gao, J., Chen, P., Wu, L., Yu, B. & Qian, L. A review on fabrication of blazed gratings. J. Phys. D: Appl. Phys. 54, 313001 (2021).

9. Li, H. et al. Relationship between machining accuracy and optical properties of convex blazed grating in ultra-precision cutting. Opt. Express 31, 36845-36858 (2023).

10. Fantova, J. et al. Single-step fabrication of highly tunable blazed gratings using triangular-shaped femtosecond laser pulses. Micromachines 15, 711 (2024).

11. Wang, Y. et al. Design of 4.7 μm High-Efficiency Hybrid Dielectric Reflection Gratings. Micromachines 13, 632 (2022).

12. Fang, X., Ren, H. & Gu, M. Orbital angular momentum holography for high-security encryption. Nat. Photonics 14, 102-108 (2020).

13. Hu, Y. et al. Trichromatic and tripolarization-channel holography with noninterleaved dielectric metasurface. Nano Lett. 20, 994-1002 (2019).

14. Li, S.-Q. et al. Phase-only transmissive spatial light modulator based on tunable dielectric metasurface. Science 364, 1087-1090 (2019).

15. Zhu, W., Xiao, F., Kang, M. & Premaratne, M. Coherent perfect absorption in an all-dielectric metasurface. Appl. Phys. Lett. 108 (2016).

16. Xu, Z. et al. Quantitatively correlated amplitude holography based on photon sieves. Adv. Opt. Mater. 8, 1901169 (2020).

17. Balthasar Mueller, J., Rubin, N. A., Devlin, R. C., Groever, B. & Capasso, F. Metasurface polarization optics: independent phase control of arbitrary orthogonal states of polarization. Phys. Rev. Lett. 118, 113901 (2017).

18. Rubin, N. A., Shi, Z. & Capasso, F. Polarization in diffractive optics and metasurfaces. Adv. Opt. Photonics 13, 836-970 (2022).

19. Xiong, B. et al. Breaking the limitation of polarization multiplexing in optical metasurfaces with engineered noise. Science 379, 294-299 (2023).

20. Yu, S., Li, L., Shi, G., Zhu, C. & Shi, Y. Generating multiple orbital angular momentum vortex beams using a metasurface in radio frequency domain. Appl. Phys. Lett. 108 (2016).

21. Ding, F., Pors, A. & Bozhevolnyi, S. I. Gradient metasurfaces: a review of fundamentals and applications. Rep. Prog. Phys. 81, 026401 (2017).

22. Zhu, R. et al. Phase-to-pattern inverse design paradigm for fast realization of functional metasurfaces via transfer learning. Nat. Commun. 12, 2974 (2021).

23. Dorrah, A. H. & Capasso, F. Tunable structured light with flat optics. Science 376, eabi6860 (2022).

24. He, G. et al. Multiplexed manipulation of orbital angular momentum and wavelength in metasurfaces based on arbitrary complex-amplitude control. Light Sci. Appl. 13, 98 (2024).

25. Ha, S. T. et al. Optoelectronic metadevices. Science 386, eadm7442 (2024).

26. Pahlevaninezhad, M. et al. Metasurface-based bijective illumination collection imaging provides high-resolution tomography in three dimensions. Nat. Photonics 16, 203-211 (2022).

27. Juliano Martins, R. et al. Metasurface-enhanced light detection and ranging technology. Nat. Commun. 13, 5724 (2022).

28. Yang, Y. et al. Integrated metasurfaces for re-envisioning a near-future disruptive optical platform. Light Sci. Appl. 12, 152 (2023).

29. Ra'di, Y., Sounas, D. L. & Alù, A. Metagratings: Beyond the limits of graded metasurfaces for wave front control. Phys. Rev. Lett. 119, 067404 (2017).

30. Faraji-Dana, M. et al. Hyperspectral imager with folded metasurface optics. ACS Photonics 6, 2161-2167 (2019).

31. Ra'di, Y. & Alù, A. Reconfigurable metagratings. ACS Photonics 5, 1779-1785 (2018).

32. Zhu, A. Y. et al. Compact aberration-corrected spectrometers in the visible using dispersion-tailored metasurfaces. Adv. Opt. Mater. 7, 1801144 (2019).

33. Ribot, C. et al. Broadband and efficient diffraction. arXiv preprint arXiv:1306.5432 (2013).

34. Deng, Z. L., Li, F. J., Li, H., Li, X. & Alù, A. Extreme diffraction control in metagratings leveraging bound states in the continuum and exceptional points. Laser Photonics Rev. 16, 2100617 (2022).

35. Li, X. et al. Independent light field manipulation in diffraction orders of metasurface holography. Laser Photonics Rev. 16, 2100592 (2022).

36. Song, X. et al. Selective diffraction with complex amplitude modulation by dielectric metasurfaces. Adv. Opt. Mater. 6, 1701181 (2018).

37. Wang, Y. et al. Perfect control of diffraction patterns with phase-gradient metasurfaces. ACS Appl. Mater. Interfaces 14, 16856-16865 (2022).

38. Deng, Z.-L., Cao, Y., Li, X. & Wang, G. P. Multifunctional metasurface: from extraordinary optical transmission to extraordinary optical diffraction in a single structure. Photonics Res. 6, 443-450 (2018).

39. Yang, R. et al. Terahertz silicon metagratings: high-efficiency dispersive beam manipulation above diffraction cone. Laser Photonics Rev. 17, 2200975 (2023).

40. Cordaro, A. et al. Solving integral equations in free space with inverse-designed ultrathin optical metagratings. Nat. Nanotechnol. 18, 365-372 (2023).

41. Zang, G., Liu, Z., Feng, S. & Zhu, W. A Polarization-Insensitive and Adaptively-Blazed Meta-Grating Based on Dispersive Metasurfaces. Laser Photonics Rev. 19, 2401031 (2025).

42. Chen, W. T. et al. Dispersion-engineered metasurfaces reaching broadband 90% relative diffraction efficiency. Nat. Commun. 14, 2544 (2023).

43. Zhou, Y. et al. Multilayer noninteracting dielectric metasurfaces for multiwavelength metaoptics. Nano Lett. 18, 7529-7537 (2018).

44. Dong, S. et al. Broadband depolarized perfect Littrow diffraction with multilayer freeform metagratings. Optica 10, 585-593 (2023).

45. Dorrah, A. H., Park, J.-S., Palmieri, A. & Capasso, F. Free-standing bilayer metasurfaces in the visible. Nat. Commun. 16, 3126 (2025).

46. Zhou, Y. et al. Multifunctional metaoptics based on bilayer metasurfaces. Light Sci. Appl. 8, 80 (2019).

47. Li, X. et al. Polarization-independent two-dimensional dielectric grating for 3× 3 beam splitter. Opt. Lasers Eng. 177, 108158 (2024).

48. Kim, K. et al. Multi-objective optimization of dynamic VO2 metagrating: broadband polarization-independent transmission modulator. Opt. Express 32, 32680-32690 (2024).

49. Yu, N. et al. Light propagation with phase discontinuities: generalized laws of reflection and refraction. science 334, 333-337 (2011).

Figures and tables

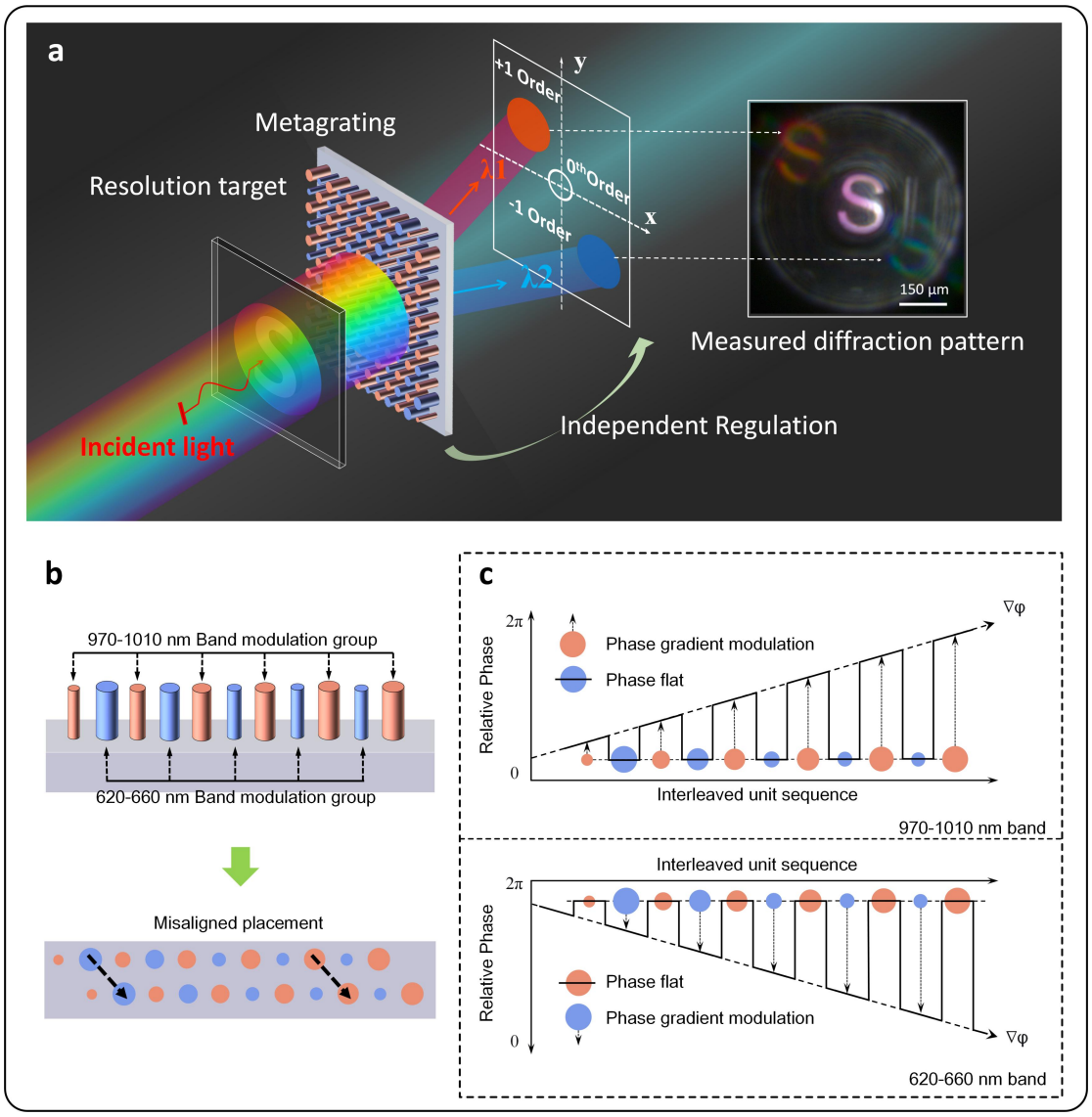


Fig. 1. Schematic illustration of the working principle and structure of the interleaved–staggered dual-band blazed metagrating. a Schematic overview of wavelength-selective diffraction control achieved by the dual-band blazed metagrating. Under normal incidence, transmitted beams at different operating bands are directed into different diffraction-order directions, achieving spatial separation. The right inset shows the corresponding experimentally measured far-field diffraction patterns. **b** Schematic illustrations of two types of functional units designed for the near-infrared band (960–1010 nm) and the visible band (620–660 nm), respectively. The two types of units are arranged in an interleaved manner and further staggered to form an extended supercell structure. **c** Schematic illustration of the effective phase modulation at different operating bands. The upper panel corresponds to the near-infrared band. In this case, the near-infrared units provide a linear phase gradient, while the visible-light units exhibit an approximately flat phase response. The lower panel corresponds to the visible band, where the modulation roles of the two unit types are reversed. As a result, opposite effective

phase gradients are formed in different bands, leading to blazed diffraction into opposite orders at dual wavelengths.

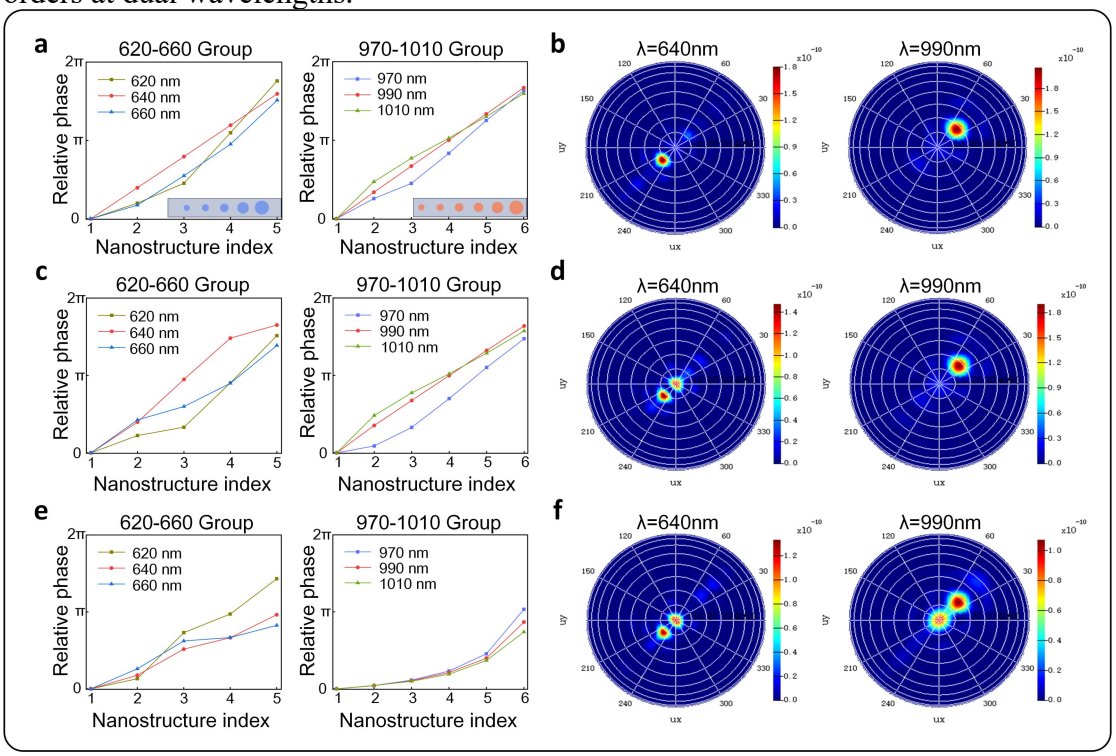


Fig. 2. Dual-band phase responses and blazed diffraction behaviors under different phase-coverage conditions. a , c , and e show the relative transmission phase distributions of the metagrating in the visible band (620–660 nm) and the near-infrared band (960–1010 nm) for three representative sets of unit parameters. The corresponding unit-sequence geometries and phase values are provided in the Supporting Information Tables S1–S6. **b , d , and f** present the corresponding far-field angular distributions at the representative wavelengths of $\lambda = 640$ nm and $\lambda = 990$ nm. **b** corresponds to the single-blaze operating state, where the transmitted energy is mainly concentrated in the −1st anomalous diffraction order at 640 nm and in the +1st order at 990 nm, yielding a single dominant lobe in both bands. **d** represents a hybrid blazed state, in which the transmitted energy at 640 nm is distributed between the 0th and −1st diffraction orders, while a single-blaze response into the +1st order is preserved at 990 nm. **f** corresponds to the dual-band partial-blaze state, where the transmitted energy at 640 nm is distributed between the 0th and −1st orders, and at 990 nm between the 0th and +1st orders.

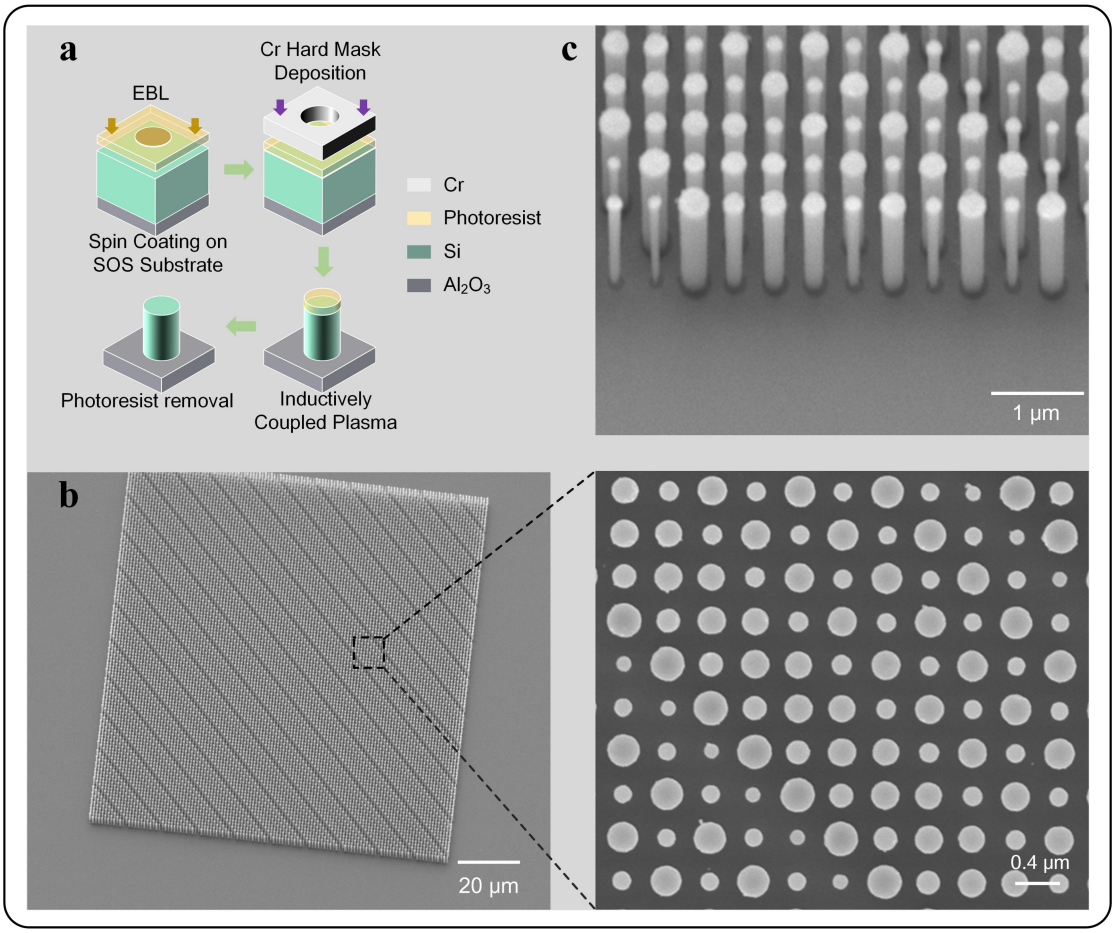


Fig. 3. Fabrication process and structural characterization of the metagrating. a Schematic illustration of the metagrating fabrication process. **b** SEM image of the fabricated metagrating; the right inset shows an enlarged top-view of the silicon nanopillars. **c** Tilted-view SEM image showing vertical profiles and smooth sidewalls.

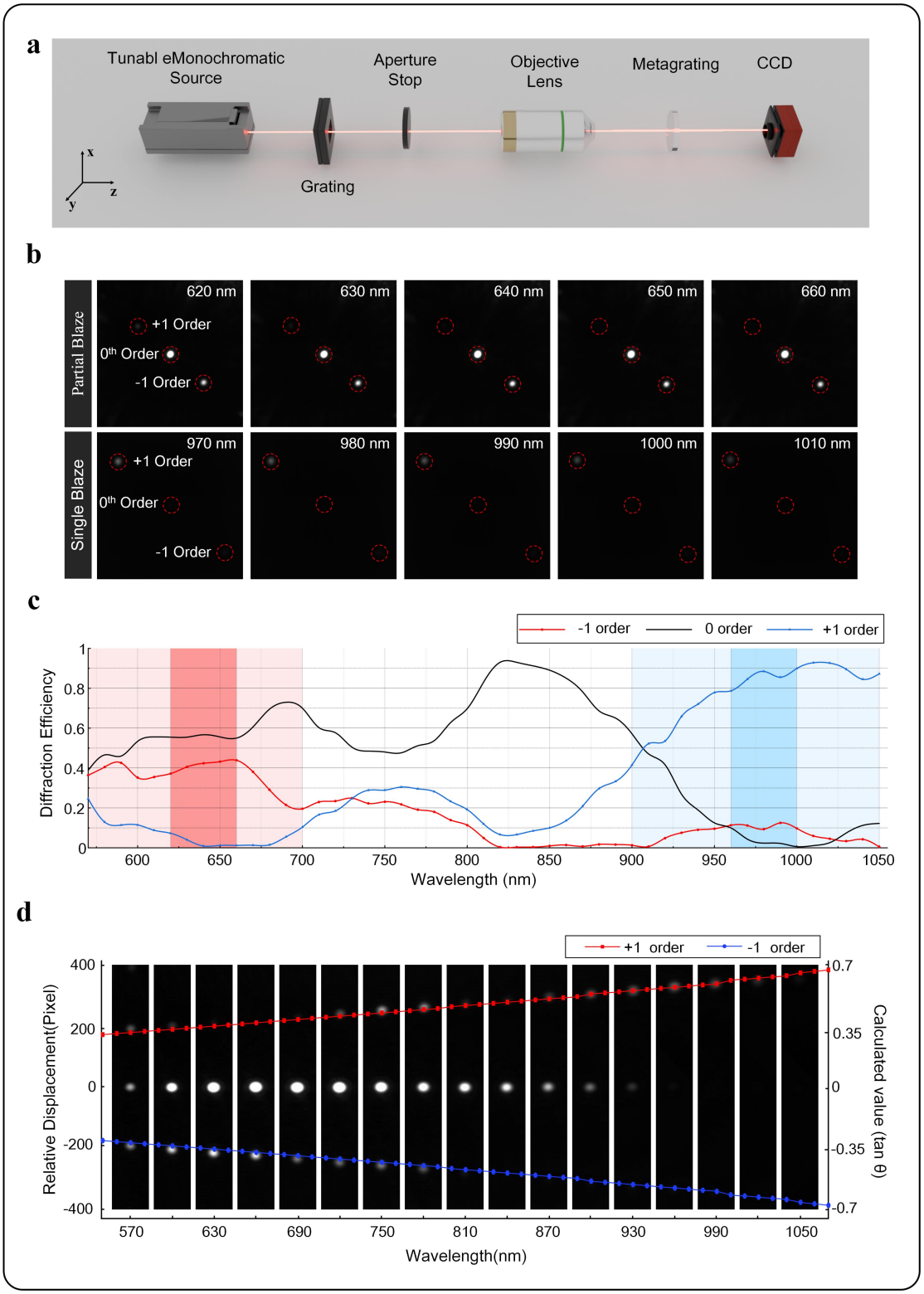


Fig. 4. Experimental setup and diffraction characterization of the metagrating. a Schematic of the optical setup for metagrating characterization. Tunable monochromatic light passes through a grating, an aperture, and an objective lens before illuminating the metagrating, and the diffracted beams are recorded by a CCD camera. **b** Measured diffraction patterns at two representative wavelength ranges: a partial-blaze mode in the

visible band (620–660 nm) and a single-blaze mode in the near-infrared band (960–1010 nm). **c** Relative diffraction efficiency spectra of the −1st, 0th, and +1st diffraction orders as functions of wavelength. The shaded regions indicate the wavelength ranges shown in (b). **d** Experimental and calculated wavelength-dependent displacements of the −1st and +1st diffraction spots relative to the 0th-order spot.

Supplementary Information

This file includes:

Table S1 to S6

Figs. S1 to S9

Equation S1

Supplementary Files

This is a list of supplementary files associated with this preprint. Click to download.

- SupplementaryInformation.pdf